

## Experimental and Computational Analysis of Bio-Inspired Winglets for Micro Air Vehicles

A. Sathyabhama, A. M. Rajiv, I. Sai Sandeep, S. S. Sandeep Kumar and C. H. Akash

*National Institute of Technology Karnataka, Surathkal, 575 025, India*

†Corresponding author email: [bhama72@gmail.com](mailto:bhama72@gmail.com)

(Received September 21, 2020; accepted February 21, 2021)

### ABSTRACT

Micro Air Vehicles (MAVs) are increasingly being used for civil and military surveillance. As the surveillance requirements are increasing, improving the range of MAVs becomes imperative. The performance of MAVs can be improved if the induced drag due to wingtip vortices can be reduced. In the present study, we try to decrease the induced drag caused by the wingtip vortices, which makes up a major part of the total drag, by introducing a winglet. A unique yet simple design, which has not yet been studied thoroughly, is explored. Inspiration is taken from the feather structures of birds to design the proposed winglet. The performance of a fixed-wing MAV at a free stream velocity ( $U_\infty$ ) of 20 m/s is studied. Multiple winglet configurations are used to compare the results with the baseline wing. An incompressible, steady three-dimensional simulation is carried out using the  $k-\omega$  SST turbulence model. The experimental studies carried out for the baseline wing matched well with those obtained from CFD. Since the numerical model is valid, only computational study is done for the modified wing. The stall angle of the baseline wing is around  $26^\circ$ . Numerical results show that when the proposed winglet is used, the stall angle for the wing is increased to around  $32^\circ$ . The use of the winglet did not produce a considerable advantage at the lower Angle of Attack (AOA), but at higher AOA, the lift coefficient ( $C_L$ ) was considerably higher. The overall drag coefficient ( $C_D$ ) was higher at lower AOA when the winglet is used. But at AOAs greater than  $5^\circ$ , the  $C_D$  reduced. Other effects of the winglet are addressed in terms of improvement in Lift-to-Drag ratio ( $L/D$ ) and reduction in vorticity. The effect of the location and number of the feathers was studied to come up with an optimum winglet configuration. The experiments were carried for the wing with optimum winglet configuration and the results agreed fairly with the numerical results.

**Keywords:** MAV; Winglet; Induced drag; Stall delay.

### NOMENCLATURE

2D	two dimensional	$V_L$	voltage generated corresponding to lift force
3D	three dimensional	$y$	absolute distance from the wall
AOA	Angle of Attack	$y^+$	non dimensional wall distance
$C_L$	lift coefficient		
$C_D$	drag coefficient		
$C_{du}$	uncorrected drag coefficient		
$C_p$	coefficient of pressure		
$c$	chord		
CFD	Computational Fluid Dynamics		
$h$	cross-sectional tunnel height		
$h_m$	manometer head		
$k$	turbulent kinetic energy		
LAR	Low Aspect Ratio		
$L$	lift force		
$L/D$	lift to drag ratio		
MAC	Mean Aerodynamic Chord		
MAV	Micro Air Vehicle		
$N$	RPM of axial flow fan unit		
RANS	Reynolds Averaged Navier Stokes		
Re	Reynolds number		
			<b>Greek Symbols</b>
		$\alpha$	angle of attack
		$\gamma$	intermittency
		$\omega$	specific rate of dissipation of k
		$\varepsilon$	turbulent dissipation
		$\varepsilon_{sb}$	solid blockage
		$\varepsilon_t$	total correction
		$\varepsilon_{wb}$	wall blockage
		$t$	model thickness
		$U_\infty$	free stream velocity
		$u_\tau$	friction velocity
		UAV	Unmanned Aerial Vehicle
		$V$	test section velocity
		$\nu$	kinematic viscosity of air
		$\tau_w$	wall shear stress

$Re_\theta$	momentum thickness Reynolds number	$\rho$	fluid density
SA	Spallart Allmaras	$\lambda_s$	shape factor
SST	Shear Stress Transport	$\sigma$	correction factor

## 1. INTRODUCTION

Micro air vehicles (MAVs) are small aircraft with a wingspan of 150 mm and a maximum take-off weight of 500 g. MAVs have a wide range of applications like surveillance, armed attacking, search and rescue operations, scientific research and transportation. Due to their low weight and sizes, they are very suitable for military surveillance applications and video recording. Due to their small size, the probability of being intercepted by radar is also low. More recently, MAVs are being used to study and analyse the growth and effects of wildfires, which has become a major crisis around the world. MAVs can be deployed in confined spaces where it is arduous for bigger Unmanned Aerial Vehicles (UAVs) to operate. There is a variety of MAVs, the two most widely used ones being fixed-wing and flapping-wing MAVs. The fixed wing MAVs have higher flight velocity and longer endurance when compared to their flapping wing counterparts. The fixed wing MAVs operate in a low Reynolds number (Re) regime, typically  $10^4$ - $10^5$  (Xiao *et al.* 2016), where many complex flow phenomena take place.

Recently, there have been many studies on MAVs due to their increased effectiveness and range of applications. Experimental studies of MAV wing performance have been carried out and documented by several authors. Pelletier and Mueller (2000) conducted wind tunnel experiments on a Low Aspect Ratio (LAR), cambered plate wings. Re was varied from 60,000 to 200,000. It was concluded that cambered wings provide better aerodynamic characteristics than at-plate wings, which is intuitive. The important result from his study is that the level of turbulence in the wind tunnel and trailing edge geometry has little effect on the measured lift coefficient ( $C_L$ ) and drag coefficient ( $C_D$ ) values for thin wings. Torres and Mueller (2004) experimentally studied the aerodynamic characteristics of wings of aspect ratio between 0.5 and 2.0 at a Re of 200,000. It was observed that wings with an aspect ratio of less than 1.25 had non-linear lift curves. These LAR wings were also observed to have high maximum  $C_L$  and the corresponding AOA. Inverse Zimmerman planform was concluded to be the most efficient in terms of L/D ratios.

Computational Fluid Dynamics (CFD) has been used by various researchers for studying the performance of MAV, as it provides a reliable solution for modeling viscous effects as well. One of the important things in a CFD simulation is selecting the correct turbulence model. Since the flow involved is of low Re, complex phenomena like flow separation and formation of separation bubbles on the wing surface are dominant characteristics of the flow. Aftab *et al.* (2016) conducted an extensive study on the NACA4415

airfoil, which is widely used for MAV and UAV applications for a flow of Re 120,000. Different turbulence models like the one-equation Spallart Allmaras (SA), two-equation k- $\omega$  SST, three-equation intermittency ( $\gamma$ ) SST, k-kl- $\omega$  and the four-equation  $\gamma$ -Re $\theta$  SST were used to model the flow around the airfoil at different AOA ranging from  $6^\circ$  to  $18^\circ$ . The results from these models were compared based on coefficient of pressure ( $C_p$ ) plots, boundary layer profiles and velocity contours. The results suggested that for fully turbulent cases, the k- $\omega$  SST model produces the most reliable results and takes the least simulation time when compared to other models. Shetty *et al.* (2013) studied two different MAV fixed-wing configurations numerically and experimentally for a range of AOA from  $4^\circ$  to  $30^\circ$ . The simulations were carried out in ANSYS Fluent for a Re of 200,000 and the results were validated using experimental results. Three different turbulence models, namely, k- $\omega$  SST, k- $\epsilon$ , and SA, were used and the results were compared. It was observed that the k- $\epsilon$  model overestimated the values of  $C_L$  and  $C_D$  compared to the experimental results. The simulations using the k- $\omega$  SST and SA models were seen to produce results similar to those obtained from experiments.

As studied by Xiao *et al.* (2016), in 3D (LAR) wings, the wingtip vortices occupy a large portion of the suction surface. The wingtip vortex and its interaction with boundary layer separation may induce strong 3D flow phenomena which do not exist on the 2D airfoils. To study this complex flow phenomenon, simple turbulence models like k- $\epsilon$  might not be adequate. In such cases, the k- $\omega$  SST model is recommended. They concluded that the flow patterns on the suction side vary strongly with AOA.

The dimensional constraint forces the MAV to use a LAR (ratio of span to chord), which will usually be in the range of 1. This LAR can be advantageous since it can offer higher stall angles compared to conventional large aspect ratio wings but also experiences higher induced drag due to wingtip vortices. The effect of the induced drag increases with an increase in AOA. For an aircraft that is used in military operations, maximizing the flight time and range is of major importance. Optimizing L/D ratio yields increased cruise range and overall better performance. In MAVs, one of the major problems faced is to increase the L/D ratio. In order to increase this value, most designers try to decrease the drag. Winglets are known to reduce the formation of wingtip vortices and the induced drag by increasing the effective aspect ratio. Some of the early work on the effects of winglets on MAV performance was carried out by Montinen *et al.* (2003). He proposed the use of conventional winglets at the tip of the wing. MAV wings with Eppler 212 airfoil cross-section, with and without a winglet, were simulated numerically, and the results

were verified experimentally. The use of winglets was seen to increase the L/D ratio under low Re values of 50,000 and 100,000, respectively. It was also observed that the enhancement in performance is more predominant when the wing has a higher aspect ratio.

Nokhandan *et al.* (2013) experimentally studied the effects of a fence type winglet made of airfoil FX60100. The bank angle ( $\Phi$ ) and sweep angle ( $\beta$ ) were varied to determine the best combination to produce the greatest improvement in L/D ratio. A maximum improvement of 20% was seen in the L/D ratio for a bank angle of  $30^\circ$  and a sweep angle of  $86^\circ$ . There have been many investigations and experiments conducted on the shape and usage the winglets (Shelton *et al.* 2006; Smith *et al.* 2001; Tamai *et al.* 2007; Bardera *et al.* 2019; Liu *et al.* 2019; Putro *et al.* 2016)

There have also been a few studies attempting to take inspiration from biological phenomena around us to solve the issue at hand. Some birds have been observed to leave behind only minute traces of wingtip vortices when they fly. The reason for this is the peculiar shape of their wings and wingtips (Fig.1). The feathers at the tip of their wings are effective in reducing the vortices (Siddiqui *et al.* 2017). Previous designs inspired by birds led to the introduction and use of wing-grid wingtips. LaRoche and Palfy (1996) suggested the earliest known form of an adaptation of bird wings on aircraft wings. They proposed the use of a wing grid wingtip and obtained a patent for their invention.

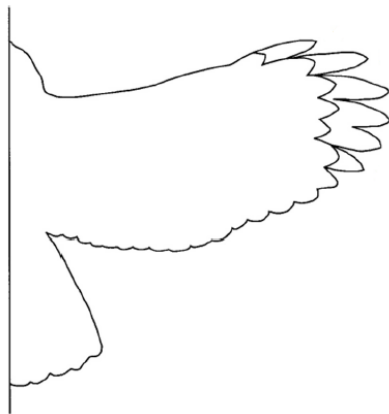


**Fig. 1. Wingtip gaps of a Harris hawk (Lynch *et al.* 2018).**

The idea of using biomimetic winglets has been around for quite a few years now and a thorough literature review on this was conducted by Siddiqui *et al.* (2017). In this review, several ways to improve MAV wing performance have been cited, like bio-mimicking the feather structure of birds or by directly attaching bird feathers onto MAV wings. A more recent effort to integrate bio-inspired wings on MAV wings was made by Ganesh *et al.* (2016). A simple yet novel winglet structure based on the feathers of bird wings was studied numerically at an AOA of  $15^\circ$  and  $20^\circ$ . It was observed that the proposed design improved the

L/D ratio at the mentioned AOA. The work seems promising but remains incomplete in multiple aspects. The results in their study lack validation of any kind, neither in the form of a mesh convergence study nor experimental data to back up their CFD results. Further, the authors failed to discuss the flow characteristics and physical causes for the improvement in performance. The parametric study performed in their research is rather arbitrary and is incomplete to a great extent. Hence there exists a research gap in this area. This is the motivation for the present work and the design has been adopted from the above mentioned study.

It was decided to use CFD to analyze the performance of the proposed winglet. The wing planform chosen for this study resembles the inverse Zimmerman planform (Chen and Qin 2013) and hence can perform well. Experimental studies are conducted at the subsonic wind tunnel facility at NITK Mangalore. The data obtained from the experiments served as a source for validating the numerical analysis.

## 2. METHODOLOGY

In the following sections, a detailed description of the experimental and numerical work done is presented.

### 2.1 Geometry

The objective of the current work is to study the effect of the bio-inspired winglet on the performance of the MAV. The MAV consists of a wing profile that is tapered and swept with the Eppeler 212 airfoil section across the span. The aspect ratio (ratio of span to centerline chord length) of the MAV is 1, which lies within the range prescribed by The American Defence Advanced Research Projects Agency (DARPA) (Kandath *et al.* 2018). It has a maximum chord length and a span of 150mm. The leading edge of the wing has a sweep of  $17^\circ$ , with a taper ratio of 0.8467 (Ganesh *et al.* 2016). The wingtip chord for this taper ratio is 127mm and the mean aerodynamic chord (MAC) is 139mm. The airfoil E212 is selected for the study as it is a cambered low Re airfoil suitable for MAV applications. The top and side views of the baseline wing are shown in Fig. 2, and those of the MAV with winglet are shown in Fig. 3.

The two parameters that can be varied are the feather width and the spacing. Feather width can be defined as shown in Fig. 4. The pitch can be defined as the distance between two identical points on two successive feathers. Spacing can be defined as the difference between pitch and width. Figure 4 shows a winglet with a feather width of 10mm with a spacing of 2mm. The feather width and spacing were varied to study and obtain an optimum configuration. The starting location of the winglet in the chordwise direction at the tip was also varied to reduce the drag penalty at lower AOA. Here, each protrusion will be referred to as a 'feather', and the entire configuration of feathers will be referred to as the 'winglet'.

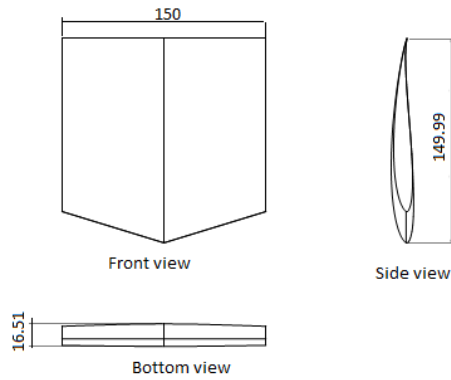


**Fig. 2. Orthographic projections of the baseline wing of E212 airfoil profile.**

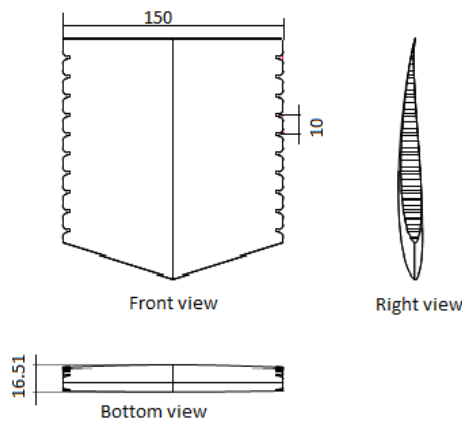


**Fig. 3. Orthographic projections of the wing with integrated winglet.**

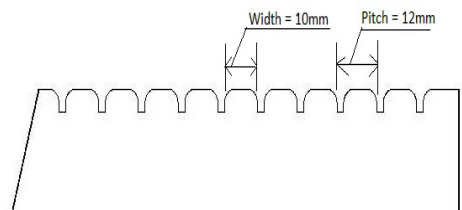


**Fig. 4. Winglet parameters.**

The models are drafted in CATIA V5R20. The airfoil profile E212 is lofted through a guideline, which is the leading edge of the wing. The profile of the airfoil at the tip is obtained using the taper ratio.

The winglet profile is generated on the baseline wing using the loft feature. The number of feathers on the tip can be controlled using the pattern feature.

## 2.2 Computational Method

The simulations are carried out on ANSYS Fluent 16.0. The baseline wing and multiple configurations of the wing with an integrated winglet are simulated and their aerodynamic performance is evaluated. The wings are simulated at a MAC Re of 188,000, corresponding to a free stream velocity of 20m/s.

## 2.3 Computational domain

Generally, for 3D aerodynamic simulations, there are two popular kinds of domain shapes used, Hemispherical and cuboidal. Previous CFD studies on MAVs used a cuboidal domain; hence the same is used in the present study as well. The distance of velocity inlet from the leading edge is taken as five times the chord length. The bottom and top boundaries of the domain are at seven times the chord length from the wing surface. The outflow boundary condition is taken at twelve times the chord length from the trailing edge. Symmetry conditions are given at seven times the chord length on either side of the wing (Fig. 5). The above mentioned dimensions were obtained from existing literature on similar studies and are inside the accepted range of dimensions (Khan *et al.* 2018; Shetty *et al.* 2013).

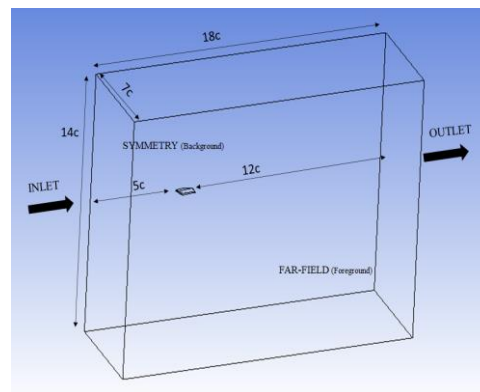


**Fig. 5. Computational domain and boundary conditions.**

## 2.4 Computational grid

The mesh is coarse towards the far-field and fine near the wing surface. The unstructured grids used for the simulations are produced using ICEM CFD 16.0. The volume elements are tetra elements and all the surface elements are tri elements. Several prism layers were generated near the wing surface to capture the high gradients in velocity and other flow variables. The first cell height for the prism layers was determined for a non-dimensional wall distance,  $y^+$  value of around one and the layers are generated such that there are 5-6 prism cells inside the viscous sublayer of the boundary (Fig. 6). The  $y^+$  value is calculated using Eq. (1).

$$y^+ = \frac{y \times u_\tau}{\nu} \quad (1)$$

where  $u_\tau$  is the friction velocity (m/s),  $y$  is the absolute distance from the wall (m),  $\nu$  is the kinematic viscosity of air ( $1.48 \times 10^{-5} \text{ m}^2/\text{s}$ ).

The friction velocity is calculated using the formula given in Eq. (2).

$$u_\tau = \left( \frac{\tau_w}{\rho} \right)^{1/2} \quad (2)$$

where  $\tau_w$  is the local wall shear stress and  $\rho$  is the fluid density, which is taken as  $1.213 \text{ kg/m}^3$ , which is the density at an altitude of 100m.

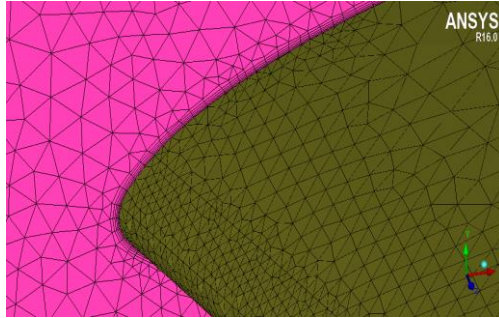


Fig. 6. Close-up view of the near-surface grid.

## 2.5 Boundary conditions

The Far-field boundary condition is treated as either inflow or outflow condition based on the direction of the convective flux. A no-slip condition is specified on the wing surface wall nodes. Symmetry condition is maintained on either side of the wing. The top and bottom boundaries are given a slip wall boundary condition for the case  $0^\circ$ AOA. The inlet face is given a velocity-inlet condition with  $U_\infty$  as 20 m/s. The outlet face is given a pressure-outlet condition with a static gauge pressure value of 0 atmospheres. The boundary conditions are shown in Fig. 5. The reference value for length is set as 0.15m, which is the centerline chord length, while that for the area is set to be  $0.01108 \text{ m}^2$ , which is the frontal area of the baseline wing. The viscosity of air is set to be  $1.86 \times 10^{-5} \text{ N-s/m}^2$ .

## 2.6 Turbulence model

The flow for a MAV has a low Re value (typically  $10^4$ - $10^5$ ). Hence it tends to experience unstable aerodynamic conditions. In such a case, it is imperative to understand flow physics in the boundary layer. The above stated are the reasons to select the Reynolds averaged Navier Stokes (RANS) SST  $k-\omega$  turbulence model. This model includes the characteristics of the wake region and the near-wall region for low Re applications. The  $k-\omega$  SST model has been used for studying MAV wings before and has been demonstrated to be effective as well (Shetty *et al.* 2013). The SST  $k-\omega$  turbulence model (Menter 1993) is a two-equation eddy-viscosity model. It is a hybrid model combining the Wilcox  $k-\omega$  (Wilcox 1988) and the  $k-\epsilon$  (Lauder and Spalding 1974) models. A blending function, F1, activates the Wilcox model near the wall and the  $k-\epsilon$  model in the free stream. This ensures that the appropriate model is utilized throughout the flow field; the  $k-\omega$  model is well suited for simulating flow in the viscous sub-layer, and the  $k-\epsilon$  model is ideal for predicting flow behavior in regions away from the wall.

## 2.7 Simulation method

A SIMPLE scheme is used for pressure-velocity coupling. The optimum values of under relaxation

factors are used for pressure, momentum and turbulent kinetic energy. Here second order discretization, second order upwind discretization and first order discretization are used for pressure, momentum and turbulent kinetic energy, respectively. The convergence criteria for the continuity equation are set as  $10^{-5}$  and that for u, v, w velocities as  $10^{-7}$ .

## 2.8 Grid Independence study

A grid independence study was taken up to validate the grid size. For this purpose, five grids of sizes 0.6 million, 0.8 million, 1.2 million, 1.4 million, and 1.7 million mesh elements were generated. The same computational setup is used to simulate the wing in all the grids at an AOA of  $6^\circ$  and the resulting  $C_L$  values and the L/D values are shown in Fig. 7. As can be seen from Fig. 7, the value of  $C_L$  is high in the case of grids consisting of 0.6 and 0.8 million elements. The  $C_L$  reaches a constant value after the mesh size exceeds 1.2 million. It was also observed that if the element count exceeded 2 million, the fluctuations in continuity residuals were high, indicating that the mesh is too fine. The simulation time per iteration also increases with an increase in element count. The same trend is observed in the values of the L/D ratio, too. Since in a CFD simulation, the computational time and resources are to be used cautiously, the grid size of 1.2 million elements is used for all further simulations in order to consume less time, without the loss of accuracy.

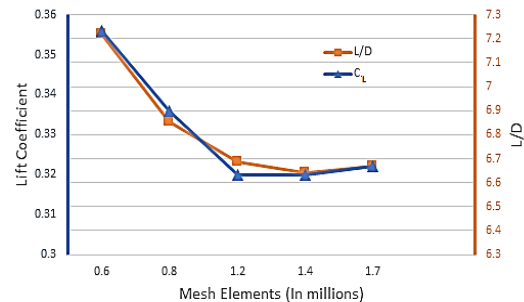


Fig. 7. Grid independence study.

## 2.9 Experimental aerodynamic study in the subsonic wind tunnel

The experimentation is performed to validate the numerical results obtained. The baseline wing model was fabricated out of wood and fixed in the test section of the wind tunnel. The test section of the open circuit, suction type tunnel measures 1m (height) x 1m (width) x 2 m (length), with a design velocity of 30 m/s and turbulence intensity of 0.5%.

Any axial or lateral turbulence is reduced and a smooth flow of air entering the test section is achieved by installing the Honeycomb and fine mesh screens for the effectiveness of the air inlet. The other specifications of the wind tunnel are shown in Table 1.

**Table 1 Wind Tunnel specifications.**

Type	Sub-sonic wind tunnel
Test section	1m (height) x 1m (width) x 2 m (length)
Air Speed (Velocity)	30 m/s
Contraction ratio	9:1
Motor capacity	11 kW(15HP), 720 RPM, 3 Phase (440 V)
Number of blades of the motor fan	6
Fan diameter	2000mm

A three component force balance was used to find the lift and drag on the wing model using the DAQ device. The strain gauges attached to the force balance are connected to the DAQ device, which gives the output. The force balance has a mechanical load transfer mechanism to strain gauged elements along with a pitching mechanism. This mechanism includes a balance calibration attachment. The wing model is attached to the plate provided on top of the force balance using four M6 screws with a cast iron base plate to maintain flatness at the point of contact. A sampling period of one second was chosen and a minimum of 500 samples were collected at each AOA and the sample size was increased to 1000 at post stall AOA. This large sampling size should give sufficiently accurate time averaged lift and drag even when the flow is unsteady. Figure 8 shows the baseline wing mounted on the force balance in the wind tunnel. The motor RPM was set according to the required flow velocity for experimentation based on the calibration chart. The measurements were taken at different AOA. The lift and drag were then used to find corresponding  $C_L$  and  $C_D$  values.



**Fig. 8. Baseline wing model attached to the force balance.**

### 2.9.1 Wind tunnel corrections

Since the flow inside a wind tunnel is bounded by its walls, it does not entirely and accurately represent the flow in an open field. To account for this effect, necessary corrections have to be incorporated into the data measured in the wind tunnel. The corrections mentioned in this section

are based on the methods given by Jewel *et al.* (1984) and Selig and McGranahan (2004). For the present study, solid blockage, wake blockage and streamline curvature corrections are considered.

Solid blockage,  $\epsilon_{sb}$ , is due to the presence of a model within the wind tunnel test section, which results in a reduction of the effective area through which the air flows. The solid blockage correction factor is calculated from Eq. (3).

$$\epsilon_{sb} = 0.822\lambda_s \frac{t^2}{h^2} \quad (3)$$

where  $t$  is the model thickness,  $h$  is the cross-sectional tunnel height and  $\lambda_s$  is the shape factor whose value is 1.2 as recommended by Jewel *et al.* (1984).

Wake blockage,  $\epsilon_{wb}$ , is caused by a decreased local pressure in the airfoil wake, which causes higher flow velocity outside the wake than the free stream. The correction factor,  $\epsilon_{wb}$ , is calculated from Eq. (4) (Selig and McGranahan 2004).

$$\epsilon_{wb} = \frac{c}{2h} C_{du} \quad (4)$$

where  $C_{du}$  is the uncorrected drag coefficient.

Streamline curvature around the airfoil is affected by wind tunnel walls and it results in induced pseudo camber of airfoil in the test section. This pseudo camber increases the lift generation. The correction factor,  $\sigma$  is calculated using Eq. (5) (Selig and McGranahan 2004).

$$\sigma = \frac{\pi^2}{48} \left( \frac{c}{2h} \right)^2 \quad (5)$$

The blockage corrections calculated using equations (3), (4), and (5) are combined to calculate the corrected parameters using Eq. (6), (7) and (8).

$$U = U_u (1 + \epsilon_t) \quad (6)$$

$$C_l = C_{lu} (1 - \sigma - 2\epsilon_t) \quad (7)$$

$$C_d = C_{du} (1 - 3\epsilon_{sb} - 2\epsilon_{wb}) \quad (8)$$

where,  $\epsilon_t = \epsilon_{sb} + \epsilon_{wb}$ . For the baseline model at an AOA of  $24^\circ$ , following values of correction factors are obtained:  $\sigma = 0.004624$ ;  $\epsilon_{wb} = 0.00617$ ;  $\epsilon_{sb} = 0.0245$ ;  $\epsilon_t = 0.03067$ .

### 2.9.2 Repeatability

In the context of experimentation, repeatability of results refers to variation in measurements taken by a single instrument or person under similar conditions. It demonstrates the reliability of experimental set up to reproduce experimental data under similar circumstances. The baseline wing model was tested in the wind tunnel on three different days at similar conditions. The results are shown in Fig. 9. The maximum variation in the measured  $C_L$  is less than 10%, implying that the experimental setup is fairly accurate and the results are repeatable.

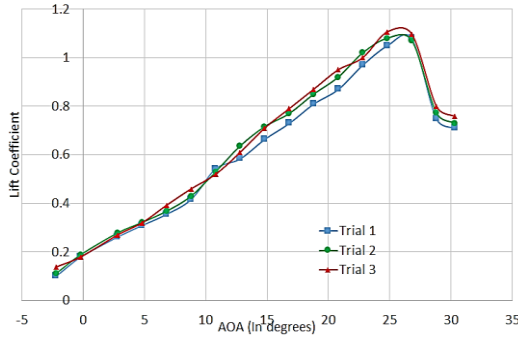


**Fig. 9. Repeatability of the experiment.**

**2.9.3 Experimental uncertainty**

The experimental uncertainties for the derived quantities calculated (Kline and McClintock 1953) for  $C_L$  and  $C_D$  is found to be  $\pm 3.56\%$  and  $\pm 4.14\%$ . The uncertainty is calculated using the following equations:

$$C_L = C_L(L, V) \tag{9}$$

But,  $L = L(\alpha, V_L)$  and  $V = V(N, h_m)$  (10)

Hence,  $C_L = C_L(\alpha, V_L, N, h)$  (11)

$$u_{c_L} = \sqrt{\left(\frac{\partial C_L}{\partial \alpha} u_{\alpha}\right)^2 + \left(\frac{\partial C_L}{\partial V_L} u_{V_L}\right)^2 + \left(\frac{\partial C_L}{\partial N} u_N\right)^2 + \left(\frac{\partial C_L}{\partial h_m} u_{h_m}\right)^2} \tag{12}$$

where, uncertainties of the independent variables are given in Table 2.

**Table 2 Independent variables and their uncertainty values.**

Variable	Uncertainty
$\alpha$	$\pm 1.03\%$
$V_L$	$\pm 0.25\%$
$N$	$\pm 0.53\%$
$h_m$	$\pm 1.32\%$

**3. RESULTS AND DISCUSSION**

This section provides the results of the experimental study and the numerical analysis and the related discussion. The baseline wing numerical results are discussed first, and inferences are drawn, which are used in further parametric study and modifications of the winglet parameters.

**3.1 Validation of Numerical results**

The comparison of numerical results with experimental results in terms of  $C_L$  and  $L/D$  ratio is shown in Fig. 10 and 11, respectively. These figures show that the numerical results are in good agreement with the experimental results. In Fig.10, the maximum deviation in  $C_L$  is 11% at  $0^\circ$ AOA. The stall AOA is correctly predicted as  $26^\circ$  by the numerical model. The post-stall values of  $C_L$  from the experiment are higher. This may be due to the streamline curvature effect at high AOAs. The deviation in the values is due to the presence of

random errors and instrument error as well. Additionally, the effect of surface roughness was not included in the numerical model.

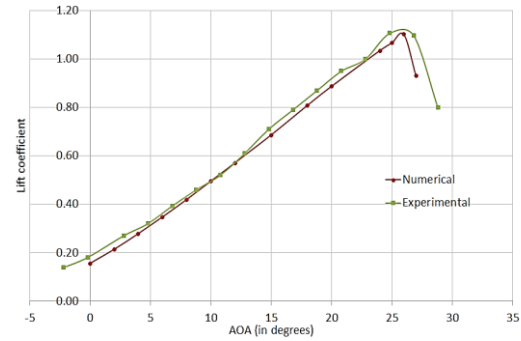


**Fig. 10. Numerical and experimental  $C_L$  vs. AOA for baseline wing.**

From Fig. 11, the maximum deviation in the  $L/D$  ratio is less than 10% throughout the range of AOAs. The  $L/D$  ratios obtained from the experiment are lower than those calculated from the numerical simulation; this is probably due to the low sensitivity of the force balance. The model weight is about 260 grams and is comparatively small. The size of the model is comparable to the structure of the force balance inside the tunnel, which might have given rise to the additional drag being measured.

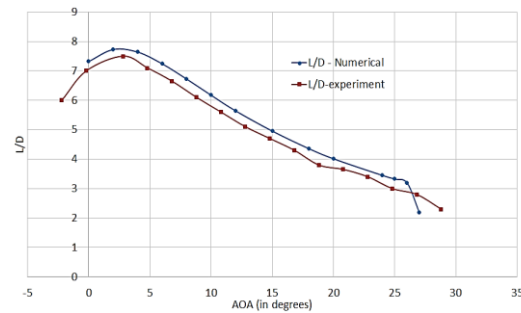


**Fig. 11. Numerical and experimental  $L/D$  vs. AOA for baseline wing.**

**3.2 Characteristics of flow over baseline wing**

As shown in the previous section, the numerical and experimental results are in good agreement, validating the numerical model being used. From the results of 3D simulations done on the baseline wing, post-processing was done to understand the flow physics over the wing. The AOAs chosen for the following illustrations are  $15^\circ$  and  $25^\circ$ . Preliminary simulation results showed that the winglet improves the performance of the wing after  $15^\circ$  and as can be seen from Fig. 10, the stall occurs at  $26^\circ$  AOA; hence  $25^\circ$  is chosen.

The pressure contour plots over the suction surface of the wing are shown in Fig. 12. There are low pressure areas near the leading edge and wingtips at  $15^\circ$  AOA as observed in Fig. 12(a). The low

pressure at the leading edge is due to the acceleration of the air over the wing. The low pressure near the tips is due to tip vortices accelerating from the pressure side to the suction side of the wing. This indicates the presence of tip vortices, although low in magnitude. From Fig. 12(b), it is evident that the pressure at the tips is lower than that at 15° AOA. This suggests stronger tip vortices and, in turn, greater induced drag. The higher pressure at the trailing edge is less predominant in the 25°AOA case, suggesting possible partial flow separation near the trailing edge.

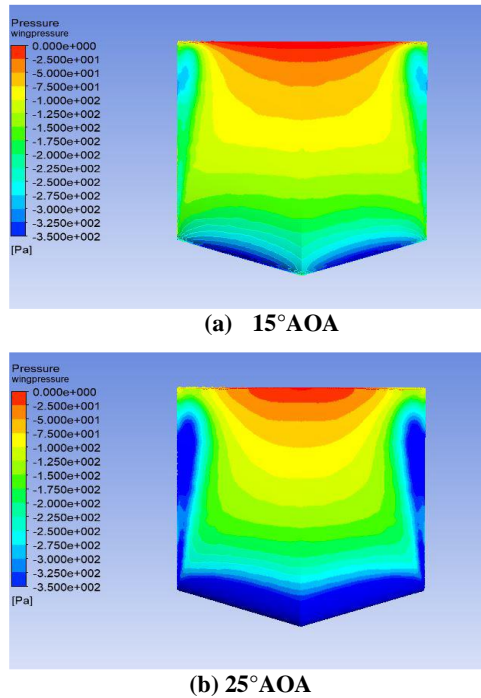


Fig. 12. Pressure contour over the wing surface.

To study the vortex formation and growth, the vorticity strength contour and flow streamlines are plotted at different chordwise locations, as shown in Fig. 13 through 15. The chordwise locations are taken to be 0.3c, 0.6c, 1c and 1.5c (wake region), respectively.

From these figures, it can be inferred that the tip vortex size and strength is larger in the case of 25°AOA. This happens because, with increasing AOA, the pressure difference between the pressure and suction side of the wing keeps increasing, thus giving rise to stronger tip vortices. These tip vortices cause induced drag, which is detrimental to the wing aerodynamic performance. At low AOAs there is no flow separation occurring on the wing. However, at higher AOAs, i.e., greater than 22°, flow separation near the trailing edge of the wing is observed. Even at higher AOA, the flow separation appears to be happening because of the 3D flow structures caused by the tip vortices interfering with the flow over the wing surface. The separation phenomenon at 25°AOA can be observed in the wing surface streamline plots, as shown in Fig. 16.

Separation is seen to occur at a location of 0.93c upstream of the wing apex. Since the wing is given a wall boundary condition, the present surface streamlines are plotted on a surface very close to the wing surface itself.

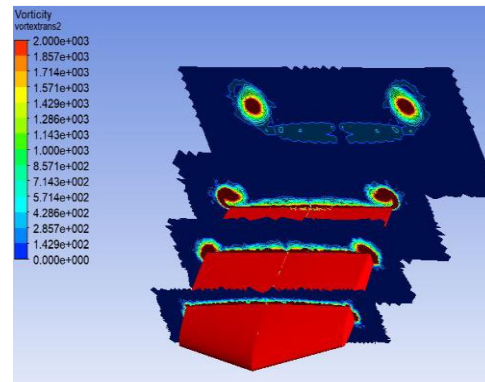


Fig. 13. Vorticity contours depicting vortex formation at 15°AOA.

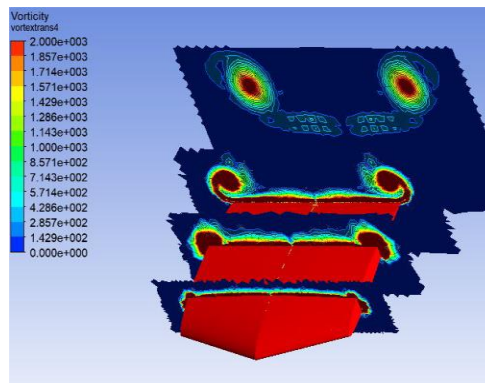
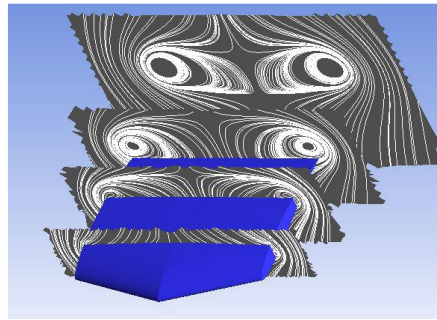


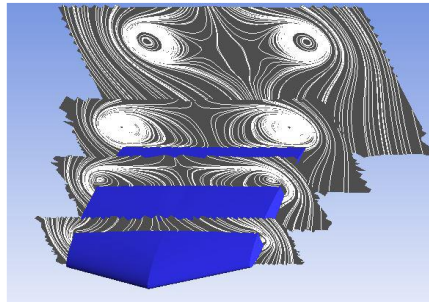
Fig. 14. Vorticity contours depicting vortex formation at 25°AOA.

Figure 16(c) shows the span-wise streamline distribution around the wing. The separation occurs where the main vortex structure detaches from the surface of the wing. After detachment, the flow structures created by the vortex interact heavily with the flow over the wing surface, thereby causing separation. Upstream of the separation location, the tip vortex is not large enough and ends on the upper surface of the wing, due to which there are widely spaced streamlines. From Fig. 12(a), it is seen that the tip vortex detaches from the wing surface only after the trailing edge. This explains Fig. 16(a), as there is no separation observed in the 15°AOA case.

The basic idea behind winglets is to reduce these tip vortices. The proposed bio-inspired winglet aims to achieve the same by modifying the flow characteristics near the wingtip. It should also be noted that badly designed winglets can, in fact, lead to a further reduction in performance, which is undesirable. For this reason, the parameters of the winglet feathers, as shown in Fig. 4, are varied and studied over a range. The results of this parametric study are discussed in the next section.

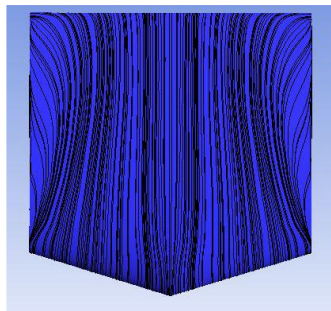


(a) 15°AOA

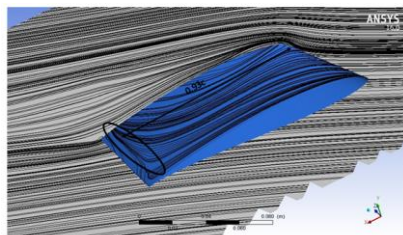


(b) 25°AOA

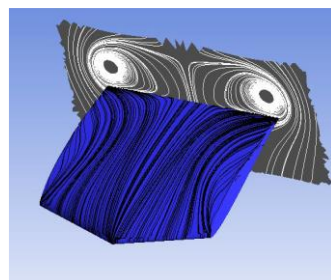
**Fig. 15. Flow streamlines depicting vortex formation.**



(a) 15°AOA



(b) 25°AOA



(c) Spanwise streamlines at 0.93c

**Fig. 16. Flow streamlines on the suction side of the wing.**

### 3.3 Winglet parametric study

The feather length and spacing are varied, as shown in Table 3. For these parameters, the value of  $C_L$  and  $L/D$  are compared to select the optimum combination. For comparison, AOA 15° is chosen for reasons explained previously, since computing lift polar for all combinations is a tedious task and requires too many machine-hours.  $L/D$  ratios are compared for each combination, since maximizing  $L/D$  is the end goal.

**Table 2 Winglet parameters.**

Feather spacing (mm)	2	4	6	8
Feather length (mm)	8	10	12	16

#### 3.3.1 Feather spacing trade study

While varying the feather spacing, the feather length was kept constant as 8 mm, chosen arbitrarily as the minimum value. The variation in  $L/D$  value with feather spacing is shown in Fig. 17.

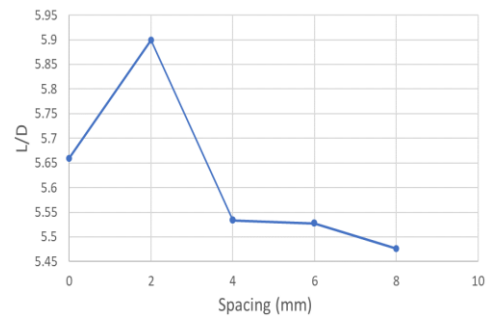


**Fig. 17. L/D v/s feather spacing.**

As can be seen from Fig. 17, the  $L/D$  ratio is highest for the spacing of 2 mm and it decreases with increased spacing. This might be due to the chronic obstruction of flow due to wider spacing resulting in more profile drag. For further analysis, the feather spacing is fixed as 2 mm.

#### 3.3.2 Feather length trade study

With a constant feather spacing of 2 mm, the feather length is varied from 8 mm to 20 mm and the corresponding  $L/D$  values are shown in Fig. 18.

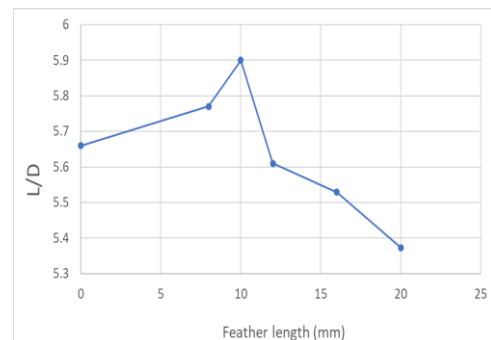


**Fig. 18. L/D v/s feather length.**

As can be seen from Fig. 18, the  $L/D$  value is higher than the baseline for feather lengths of 8 mm and 10mm, that for the latter being higher.  $L/D$  decreases as feather length is further increased. Hence, the feather length of 10 mm is used in further analysis.

### 3.4 Winglet numerical analysis

As discussed in the previous section, a feather length of 10 mm and a feather spacing of 2 mm were finalized for further study. A nomenclature for the winglet is adopted based on the feather length and spacing. The winglet with feather length 10 mm and spacing 2 mm will be referred to as W10.2 from here on. The lift polar and  $L/D$  plot of the wing with the winglet are shown in Fig. 19 and 20.

The simulations were run for different AOA until stall was observed. As seen from Fig. 19, the baseline wing has a stall AOA of around  $26^\circ$ . In contrast, the wing with the winglet is observed to exhibit stall at around  $32^\circ$ AOA, indicating stall delay when the winglet is incorporated.

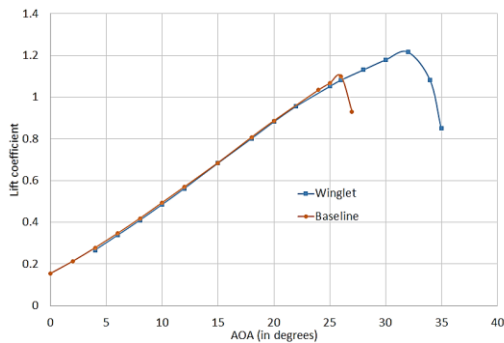


Fig. 19. Comparison of  $C_L$  for the baseline wing and W10.2.

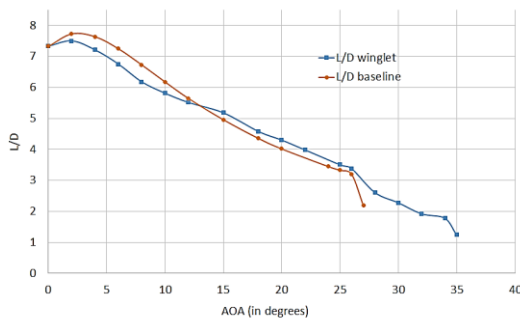
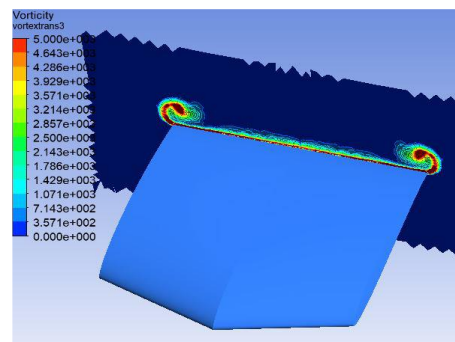


Fig. 20.  $L/D$  ratio comparison of the baseline wing and W10.2

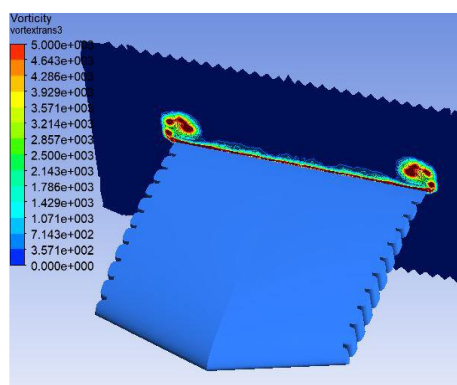
The  $C_L$  values are almost similar for the entire range of AOA till about  $26^\circ$ , after which the  $C_L$  of the wing with winglet is higher. Another important improvement can be observed when the  $L/D$  plots of both the wings are compared. It can be seen from Fig. 20, the  $L/D$  ratio of the winglet case is lower at lower AOA, but after crossing  $15^\circ$  of AOA, the drag coefficient of the wing with winglet reduces sufficiently that the overall  $L/D$  value is higher than the baseline wing. This result also seems intuitively

correct, since the induced drag due to vortices increases with increase in AOA, the winglet becomes more effective at higher AOA. Despite having a similar  $C_L$  at low AOAs, the winglet produces more drag than the baseline wing due to its complicated geometry. This extra drag is mainly profile drag. After a certain point, the increase in profile drag is compensated for by the reduction in induced drag.

A better understanding of the flow physics can be gained by studying the contours of vorticity from the results of these simulations. For the purpose of juxtaposition, the results from AOA  $15^\circ$  and  $25^\circ$  are taken to compare the change in flow phenomena occurring when the winglets are used. Figures 21 and 22 show the comparison for  $15^\circ$  and  $25^\circ$  AOA, respectively. It can be concluded faithfully by observing the vorticity contour plots near the trailing edge that the vortex strength in the flow is, in fact, affected by the presence of the winglet. In the case of  $15^\circ$  AOA, the vortex strength is seen to be slightly reduced and a bit disturbed as compared to the baseline case. In the case of  $25^\circ$  AOA, there is a considerable reduction in the vortex strength in the central region. This is the reason for the reduction in overall drag at  $25^\circ$  in the case of the wing with winglet.



(a) Baseline wing



(b) Wing with winglet

Fig. 21. Vortex strength comparison at  $15^\circ$  AOA.

From Fig. 21, it is evident that there is a profile drag penalty at lower AOAs due to the winglet. From the suction surface contours shown in Fig. 12, it can be seen that the vortex strength and the low pressure region becomes predominant only after a certain

distance from the leading edge. Thus, providing winglet feathers from the leading edge might be causing the drag penalty observed at lower AOA. Providing feathers only at the trailing edge of the wingtip can solve this problem. Thus, another parametric study was done to determine the number of feathers to be placed on the wingtip to increase the performance further. The results of this parametric study are discussed in the next section.

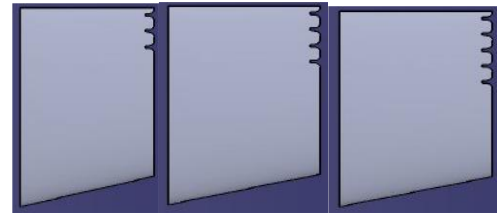
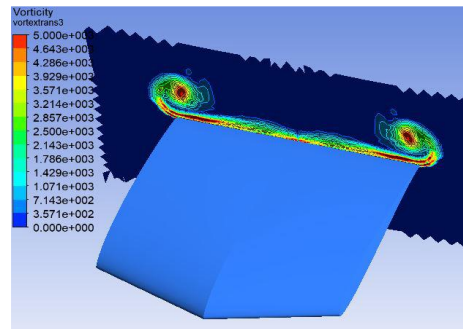
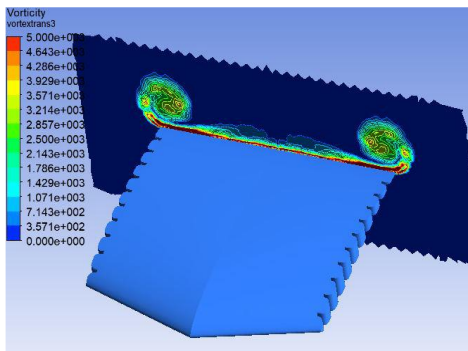


**Fig. 23. Semi-span configurations selected for the trade study.**



(a) Baseline wing



(b) Wing with winglet

**Fig. 22. Vortex strength comparison at 25° AOA.**

### 3.4.1 Feather number trade study

The feathers are provided only near the trailing edge of the wingtip and the resulting L/D ratios are compared to decide the merit of each configuration. For this study, the feather length and spacing are fixed at 10 mm and 2 mm, respectively, as stated earlier. Figure 23 shows three of the seven configurations used for the trade study. They have 2, 3 and 4 feathers at the wingtip, respectively. All the results shown are at 12°AOA.

The obtained  $C_L$  and L/D values are shown in Fig. 24 and 25, respectively. As seen from Fig. 24, the  $C_L$  increases until the point where four feathers are used and decreases as the number of feathers increases further. A similar trend is observed in the case of the L/D ratio as well, where the L/D ratio for the case of 3 and 4 feathers is almost similar, the variation is only 1%. The payload of the MAV can be increased if the  $C_L$  is high; thus, the configuration with four feathers is selected. The  $C_L$  and L/D ratio for the selected configuration is then plotted over the entire range of AOAs and compared with the baseline wing in the next section.

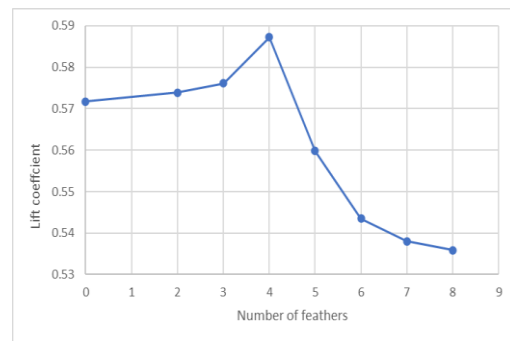


**Fig. 24.  $C_L$  v/s number of feathers.**

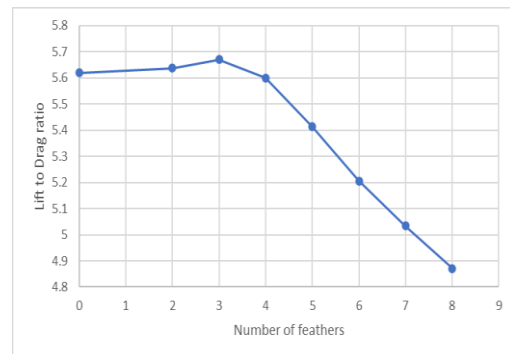


**Fig. 25. L/D v/s number of feathers.**

### 3.5 Experimental and Numerical results for final winglet configuration

Due to COVID-19 pandemic, the Institution was closed for a long period, and hence, the experiments were conducted only for the final winglet configuration. The manufacturing unit which fabricated the baseline model too was closed. So, the wing model was 3D printed on Proto center 999 3D printer available at NITK-STEP. The fused deposition modeling process of printing was used with a total processing time of 50 hours. The material used for printing is Poly Lactic Acid which is biodegradable thermoplastic material with high tensile and shear strength as required for the present work. The nozzle diameter is 0.4 mm and material diameter is 1.75 mm. The layer resolution chosen to be 200 micron and infill to be 100% material to make the weight comparable with the baseline wood model. The 3D printed wing with winglet weighed 20gms less compared to the baseline wood model. The average surface roughness ( $R_a$ ) of the wood model is  $4.97\mu\text{m}$  and that of 3D printed one is  $4.5\mu\text{m}$ . The models used for experimentation are shown in Fig. 26.



**Fig. 26. Baseline and modified wing models used for experimentation.**

The  $C_L$  and  $L/D$  plots for the final configuration of the winglet are compared with that of the baseline wing, as shown in Fig. 27 and 28, respectively. From Fig. 27, it is evident that the  $C_L$  values predicted from the numerical simulation are similar for the baseline and modified wing till an AOA of  $26^\circ$  where the baseline wing stalls. The modified wing has a stall AOA of  $32^\circ$ . But the experimental stall AOA is  $28^\circ$  and the  $C_L$  values are slightly higher than the numerical results but after the stall AOA, the values are lower than that of numerical results. At higher AOA, light vibration of the model was observed due its small size and weight. This could be the reason for the deviation between the experimental and numerical results.

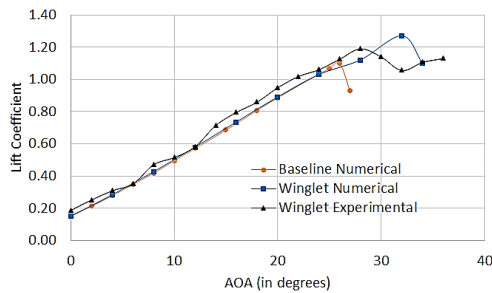


**Fig. 27. Comparison of  $C_L$  values for baseline and modified wing.**

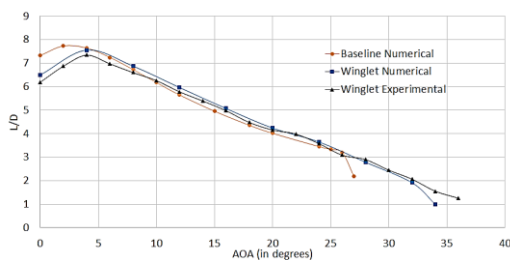
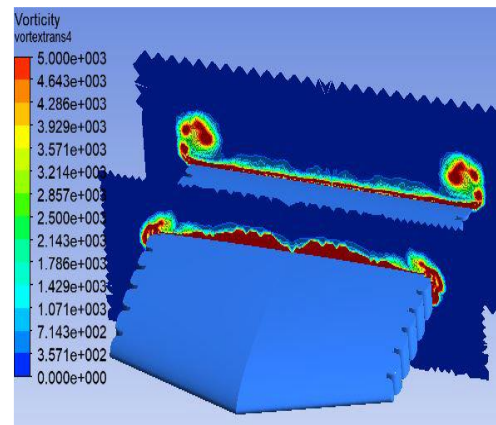


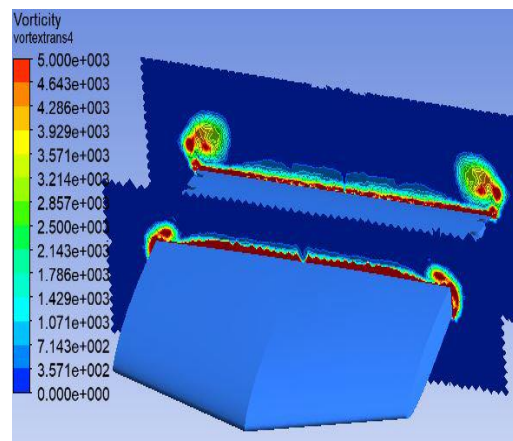
**Fig. 28.  $L/D$  comparison of baseline and modified wing.**

The experimental and numerical results follow the same trend for  $L/D$  as seen in Fig.28, the experimental values being lower than the numerical values, especially at higher AOA. This could be due to the higher drag during experimentation, as explained previously for the baseline model. The  $L/D$  comparison shown in Fig. 28 indicates that at AOA less than  $5^\circ$ , the  $L/D$  of the modified wing is less than that of the baseline wing. This is an improvement from the previous configuration where the  $L/D$  was lower for modified wing till AOA of  $15^\circ$ . The profile drag penalty at lower

AOAs is reduced to a great extent. It can also be observed that maximum  $L/D$  occurs at around  $4^\circ$  AOA for the modified wing, whereas it is at  $2^\circ$  AOA for the baseline wing. MAVs are trimmed to fly at AOA of maximum  $L/D$ . Thus, having a maximum  $L/D$  at higher AOA means a higher payload capacity of the MAV. The  $C_L$  at  $2^\circ$  AOA is 0.21 and at  $4^\circ$  is 0.283, signifying a 34% increase in cruise payload capacity. This improvement in payload capacity can be used to have bigger batteries on the MAV, increasing its range further. This improvement in  $L/D$  at lower AOA can be attributed to reduced profile drag, as stated earlier. This can be seen clearly in Fig. 29. The winglet with eight feathers is shown in Fig. 29(a) and Fig. 29(b) shows the case of the winglet with four feathers only towards the trailing edge of the wingtip. The vorticity strength contour is plotted at two chordwise locations - one at  $0.6c$  and the other at the trailing edge. The first contour is plotted at  $0.6c$ , as that is the location where the wingtip is modified in case 29(b).



(a) Winglet with 8 feathers



(b) Winglet with four feathers

**Fig. 29. Vortex strength comparison at  $15^\circ$  AOA.**

It can be seen from Fig. 29 that in the first section, the vortex structure in case 29(a) is more disturbed than in the case of 29(b). This is due to the presence of disturbances in the flow till that point. Subsequently, this reflects in the vortex strength at the trailing edge. The vortex strength in the case

with four feathers is lower than that with eight feathers. Thus, conclusively explains the improvement in performance.

#### 4. CONCLUSION

The work done to investigate this novel idea started with an extensive review of the existing literature. Numerical and experimental study of the baseline model and the final winglet configuration was carried out along with numerical analysis of the modified wing. The following points can be concluded from the present work:

The proposed winglet reduces induced drag due to the wingtip vortices by reducing the vortex strength.

The optimum winglet configuration is obtained with a feather length of 10 mm and a spacing of 2mm, with four feathers towards the trailing edge of the wingtip.

The pressure distribution on the suction surface of the wing is similar with and without the winglet. This is the reason for similar  $C_L$  values.

The stall AOA of the baseline wing is  $26^\circ$  and when the winglet is used, the stall AOA is shifted to  $32^\circ$ .

The performance of the wing is further improved by providing winglet feathers only towards the trailing edge of the wingtip. This is done to reduce the profile drag penalty at lower AOA.

The L/D of the wing with the winglet is higher than the baseline wing for AOA's higher than  $5^\circ$ . A maximum improvement in L/D of 6.87% is observed at an AOA of  $15^\circ$ . A similar improvement is observed in the AOA range of  $12^\circ$  to  $16^\circ$ .

Flow separation on the wing occurs at remarkably high AOA, around  $22^\circ$ . The separation is likely caused by the flow structures created by the wingtip vortices interacting with the flow over the wing.

Good agreement between experimental and numerical results was observed both for baseline wing and optimized wing with winglet.

#### ACKNOWLEDGEMENTS

Authors would like to acknowledge the financial support extended by the Science & Engineering Research Board (SERB), India (Sanction order: EMR/2015/000879) to carry out this research work.

#### REFERENCES

Aftab, S. M., A. S. Rafie, N. A. Razak and K. A. Ahmad (2016) Turbulence Model Selection for Low Reynolds Number Flows. *PLoS One* 11(4), e0153755.

Autodesk, C. (2019). SST k-omega turbulence model.

Bardera, R., E. Barroso and A. Rodriguez (2019).

Experimental determination of profile and induced drag components in a biomimetic design MAV with grids. *AIAA Aviation*. Dallas Texas.

Chen, J. Z. and N. Qin (2013). Planform Effects for Low-Reynolds-Number Thin Wings with Positive and Reflex Cambers. *Journal of Aircraft* 50(3), 952-964.

Ganesh, K., S. K. Aravindh Kumar and J. Jamuna Kumari (2016). Numerical Analysis of Flow Over Fixed Wing Mav with Bio Inspired Winglets. *International Journal of Engineering Research* 5(5), 79-84.

Jewel, B. B., W. Rae and A. Pope (1984). *Low-speed wind tunnel testing*, Wiley.

Kandath, H., J. V. Pushpangathan, T. Bera, S. Dhall, and M. S. Bhat (2018). Modeling and closed loop flight testing of a fixed wing micro air vehicle. *Micromachines* 9 (3), 1-22.

Khan, M., C. Padhy, M. Nandish and K. Rita (2018). Computational Analysis of Bio-Inspired Corrugated Airfoil with Varying Corrugation Angle. *Journal of Aeronautics & Aerospace Engineering* 07, 10-13.

Kline, S. J. and F. A. McClintock (1953) Describing uncertainties in single-sample experiments, *Mechanical Engineering* 75(1), 3-8.

La Roche, U. and S. Palffy (1996). Wing-grid, a novel device for drag reduction in wings. *Proceedings of ICAS 96*.

Lauder, B. and D. Spalding (1974). The numerical computation of turbulent flows. *Computer Methods in Applied Mechanics and Engineering* 3(2), 269-289.

Liu, Q., Q. Li, X. Zhou, P. Xu, L. Ren and S. Pan (2019). Development of a novel flapping wing micro aerial vehicle with elliptical wingtip trajectory. *Journal of Mechanical Sciences* 10(2), 355-362

Lynch, M., B. Mandadzhiev and A. Wissa (2018) Bioinspired wingtip devices: A pathway to improve aerodynamic performance during low Reynolds number flight, *Bioinspiration and Biomimetics* 13, 036003.

Menter, F. (1993). Zonal Two Equation k- $\omega$  Turbulence Models for Aerodynamic Flows. *AIAA Journal*, 2906.

Monttinen, J., H. Reed, K. Squires and W. Saric (2003). On the Effect of Winglets on the Performance of Micro-Aerial-Vehicles. *1<sup>st</sup> ASU Symposium on Research in Engineering and Applied Sciences* 01, 1-7.

Nokhandan, M. M., A. Hashemi and A. Sedaghat (2013). Design and simulation of an efficient winglet to enhance aerodynamic performance of a MAV. *21<sup>st</sup> Annual International Conference on Mechanical Engineering*, Tehran.

- Pelletier, A. and T. J. Mueller (2000) Low Reynolds Number Aerodynamics of Low Aspect Ratio, Thin/Flat/Cambered-Plate Wings *Journal of Aircraft* 37(5), 825.
- Putro, H. S., S. Sutardi and A. Wawan (2016). Numerical Study of Aerodynamic Analysis on Wing Airfoil NACA 43018 with the addition of Forward and Rearward Wingtip Fence. *Proceedings of the International Mechanical Engineering and Engineering Education Conferences*.
- Selig, M. and B. McGranahan (2004). Wind tunnel aerodynamic tests of six airfoils for use on small wind turbines, *NREL/SR-500-34515*.
- Shelton, A., A. Tomar, J. V. R. Prasad, M. Smith, N. Komerath, (2006). Active Multiple Winglets for Improved Unmanned-Aerial-Vehicle Performance. *Journal of Aircraft* 43(1), 110-116.
- Shetty, P., M. B. Subrahmanya, D. S. Kulkarni and B. N. Rajani (2013). CFD Simulation of Flow Past Micro Air Vehicle Wings. *CSIR - NAL PD*.
- Siddiqui, N. A., W. Asrar and E. Sulaeman (2017). Literature review: Biomimetic and conventional aircraft wingtips. *International Journal of Aviation, Aeronautics, and Aerospace* 4 (2), 1-25.
- Smith, M., N. Komerath, R. Ames, O. Wong and J. Pearson (2001) Performance Analysis of a Wing with Multiple Winglets. *AIAA*. 2001-2407.
- Tamai, M., Z. Wang, G. Rajagopalan, H. Hu and G. He (2007). Aerodynamic Performance of a Corrugated Dragonfly Airfoil Compared with Smooth Airfoils at Low Reynolds Numbers. *AIAA* 2007-483.
- Torres, G. E., T. J. Mueller (2004). Low-Aspect-Ratio Wing Aerodynamics at Low Reynolds Numbers. *AIAA Journal* 42(5), 865.
- Wilcox, D. C. (1988). Reassessment of the scale-determining equation for advanced turbulence models. *AIAA Journal*. 26(11), 1299.
- Xiao, T., Z. Li and S. Deng (2016). Numerical study on the flow characteristics of micro air vehicle wings at low Reynolds numbers. *International Journal of Micro Air Vehicles*. 8(1), 29-40.